Materials International
Open Access Journal (ISSN: 2668-5728)

Article
Volume 7, Issue 1, 2025, 1
https://doi.org/10.33263/Materials71.001

Structural and Optical Properties of Copper-Doped Zinc Ferrites Using Solid State Reaction Method

Vani Ankam [1], Ganesh Karka [1], Lalitha G Reddy [1,*]

[1] Department of Physics, Telangana University, Nizamabad
* Correspondence: glalithareddy@gmail.com;

Scopus Author ID: 56088618100
Received: 13.06.2024; Accepted: 6.10.2024; Published: 6.01.2025

Abstract: This study aims to investigate the structural and optical properties of copper-doped zinc ferrites ($ZnFe_2O_4$:Cu) by employing X-ray diffraction (XRD), UV-Vis spectroscopy, Raman spectroscopy, and Fourier Transform Spectroscopy (FTIR) techniques. Using the solid-state reaction technique, a series $Cu_xZn_{1-x}Fe_2O_4$ of samples with x = 0, 0.25, 0.5, 0.75, 1 were created. X-ray analysis verified the production of a single-phase cubic spinel structure for all concentrations. The X-ray diffraction pattern of copper ferrite showed a pure spinel structure with Jahn-Teller tetragonal distortion. According to Rietveld refinement, the $CuxZn_1$-xFe_2O_4 with all x concentrations corresponds to the usual spinel structure. As the concentration of copper increased, the crystal size decreased except for $Cu_{0.5}Zn_{0.5}Fe_2O_4$, which was high compared to all. The lattice parameters and the X-ray density varied. Copper-doped zinc ferrites have band gaps increased from 1.825 eV to 2.776eV. Infrared and Raman spectroscopy also confirmed the spinel phase formation in the samples. The deconvoluted Raman spectra were used to compute the locations of five Raman modes as well as intensity variations. The cationic arrangement in A and B sites was inferred using deconvoluted Raman peaks. The crystal structure is more visible in Raman spectra than in XRD at room temperature. FT-IR analysis validated the spinel structure, revealing absorption bands at 630-540 cm^{-1} and 525-390 cm^{-1} for higher and lower frequencies, respectively. Copper doping is expected to influence zinc ferrites' crystallographic structure and optical behavior, potentially enhancing their applications in various technological fields.

Keywords: copper; doping; ferrite; raman; XRD; zinc.

1. Introduction

Ferrites with a spinel structure are the most intriguing magnetic materials used in modern electrical engineering, both scientifically and practically [1]. Owing to its well-known electrical and magnetic characteristics, zinc ferrites ($ZnFe_2O_4$) are a good choice for various applications, such as sensors, catalysts, and magnetic storage systems. One can adjust their optical and structural characteristics by doping zinc ferrites with copper (Cu), tailoring their performance for certain uses. Ferrospinels' functional properties are influenced by their composition, ion valence state, magnetic properties, and distribution within their actual structure.

AB_2O_4 is a common representation for spinels, where "A" can be any divalent cation, such as Cu^{2+}, Mn^{2+}, Zn^{2+}, Ni^{2+}, Fe^{2+}, etc., and "B" can be any trivalent cation, such as Fe^{3+}, Mn^{3+}, etc. As a result of their attraction for different surroundings, A^{2+} and B^{3+}cations often occupy either the octahedral or tetrahedral sites in spinels that have a cubic symmetry with the

Fd3m space group. A normal or direct spinel network is one in which every divalent cation is found in the tetrahedral locations. An equal number of trivalent cations must occupy tetrahedral sites when octahedral sites are filled by a portion or the entirety of divalent cations under certain circumstances. The spinel structure is either totally or partly reversed in these situations [2].

The preparation technique and chemical makeup both affect this so-called cation distribution. Zinc ferrites are a type of soft ferrite material that has low losses and high magnetic permeability. These substances are widely employed in several applications, including microwave devices, These materials are widely employed in many different applications, including rod antennas, transformer cores, computer memory chips, magnetic recording media, microwave devices, and many other areas of electrical and telecommunication engineering [3–5]. The preparation technique, dopant type, and dopant concentration affect spinel ferrites' structural and optical properties.

This study focuses on characterizing these modifications using X-ray diffraction (XRD) for structural analysis, UV-Vis spectroscopy for optical properties, and Raman spectroscopy for vibrational modes. In the present work, five different compositions of copper-doped zinc ferrites have been prepared by the solid-state reaction method with the chemical formula $Cu_xZn_{1-x}Fe_2O_4$ (x = 0, 0.25, 0.5, 0.75, 1), and their structural and optical characteristics were studied at room temperature.

2. Materials and Methods

The chemical composition of Copper-Doped Zinc Ferrites $Cu_xZn_{1-x}Fe_2O_4$ (where x varies from 0 to 1). Using high-purity oxides of CuO, ZnO, and Fe_2O_3, the ferrite system $Cu_xZn_{1-x}Fe_2O_4$ (x = 0, 0.25, 0.5, 0.75, 1) was created using the solid-state reaction process [6, 7]. The molecular weight of the reagent powders was exactly determined by precision weighing. The ingredients were first thoroughly mixed for 5 hours using an agate mortar. After that, they were calcinated in a muffle furnace at 800°C for 2 h. After that, it was thoroughly mixed for 3 hours using an agate mortar to get a fine powder for mixing atoms, and the powder was compressed into the form of a disk. To create ferrite, the disk-shaped samples underwent a solid-state process of pre-sintering for 2 h at 1050°C in a muffle furnace. All of the sample surfaces were polished to eliminate any oxide layer that could have developed during the sintering process.

XRD patterns are recorded using a diffractometer with Cu-Kα radiation. The data is analyzed to identify phase purity and any shifts in peak positions or changes in peak intensities that indicate lattice distortion due to Cu doping. The Scherrer equation is used to estimate crystallite size from the peak broadening. Using CuKα radiation, a Philips Analytical X-ray diffractometer verified the formation of ferrite. The powder diffraction patterns were scanned using a scan step of 0.05 and a counting duration of 5 s/step, within the 2θ range of 20–100°. The structure of the crystal was ascertained using X-ray diffraction (XRD) data. Band gaps are calculated from Ultra-Voilet Visible (UV-VIS) spectroscopy. UV-VIS spectra were recorded at room temperature in the 200–800 nm range. Vibrational modes are observed from Raman spectroscopy. Raman spectra were recorded in 100-800 cm^{-1} range using a laser source operating at 633 nm. Vibrational characteristics were obtained from Fourier transform infrared spectroscopy (FTIR) studies. FTIR was recorded in the range 400- 4000 cm^{-1}.

3. Results and Discussion

3.1. XRD analysis.

XRD analysis involves 3 following stages, such as phase identification: The XRD patterns confirm the formation of the spinel structure typical of $ZnFe_2O_4$. Lattice parameter changes: shifts in peak positions and changes in lattice parameters are observed, indicating the successful incorporation of Cu ions into the $ZnFe_2O_4$ lattice. The crystallite size is calculated and compared across different doping levels to understand the impact of Cu on crystal growth.

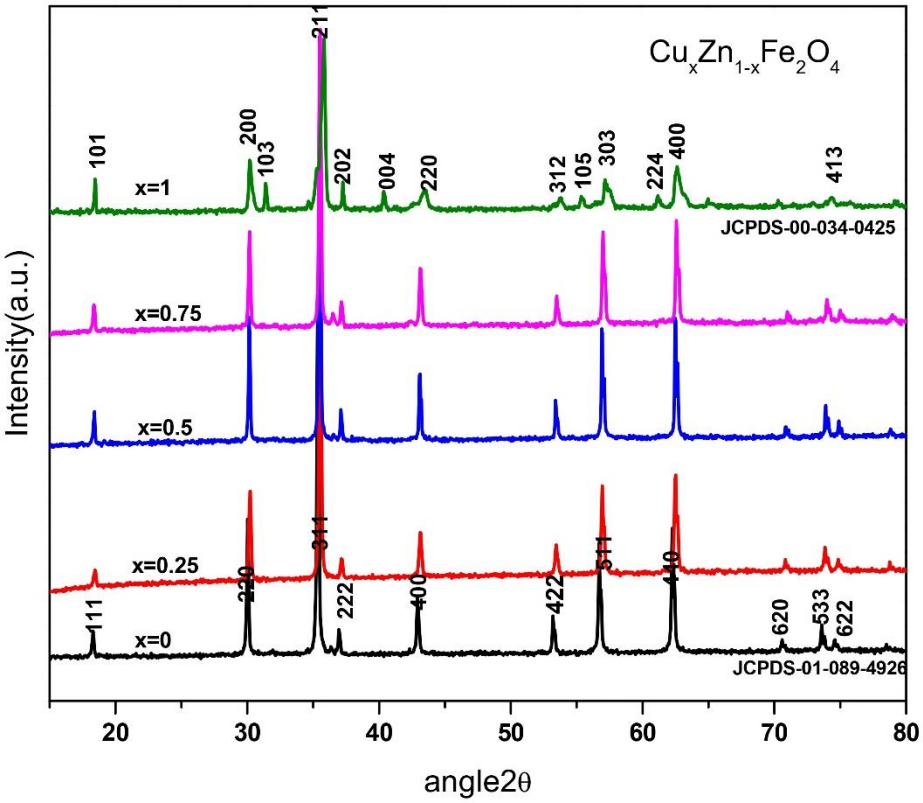

Figure 1. XRD Diffraction Patterns of $Cu_x\ Zn_{1-x}\ Fe_2O_4$ (x = 0, 0.25, 0.5, 0.75, 1).

In the given study, the XRD pattern for all of the $Cu_x\ Zn_{(1-x)}\ Fe_2O_4$ samples is displayed in Figure 1, with each peak's (h k l) values indicated. The sample's XRD pattern, which displays distinct, unambiguous reflections, shows that, aside from pure $CuFe_2O_4$, a single-phase cubic spinel structure has formed. Ferrites must have a single-phase cubic structure in order to have the best possible magnetic and transport capabilities. The spinel phase is indicated by the peaks (111), (220), (311), (222), (400), (422), (511), (440), (620), (533), and (622). All diffraction peaks are matched with JCPDS-01-089-4926. $CuFe_2O_4$ in pure form showed an ideal tetragonal structure followed by the peaks (101), (200), (211), (202), (004), (220), (312), (105), (303), (224), (400). For $CuFe_2O_4$, all diffraction peaks are matched with JCPDS-00-034-0425. Debye Scherrer's formula was used to determine the average crystallite size for each sample with respect to the high-intensity peak plane (311) for pure zinc ferrite and copper-doped zinc ferrite (211) for copper ferrite. The John-Teller phenomenon has been used to explain the tetragonal distortion of $CuFe_2O_4$, which is a deformed inverse spinel [8]. The authors have shown that tetragonal deformation has been seen at higher Cu concentrations (x=0, 0.25, 0.5, 0.75, 1). However, in our instance, tetragonality only manifests itself for pure copper ferrite, maybe due to a negligible quantity of tetragonal phase with a greater Cu content concurrent with the

previous research [9]. Phase transformation is due to cation distribution, as reported [6]. One can express the Debye-Scherrer formula to determine the size of the crystallite.

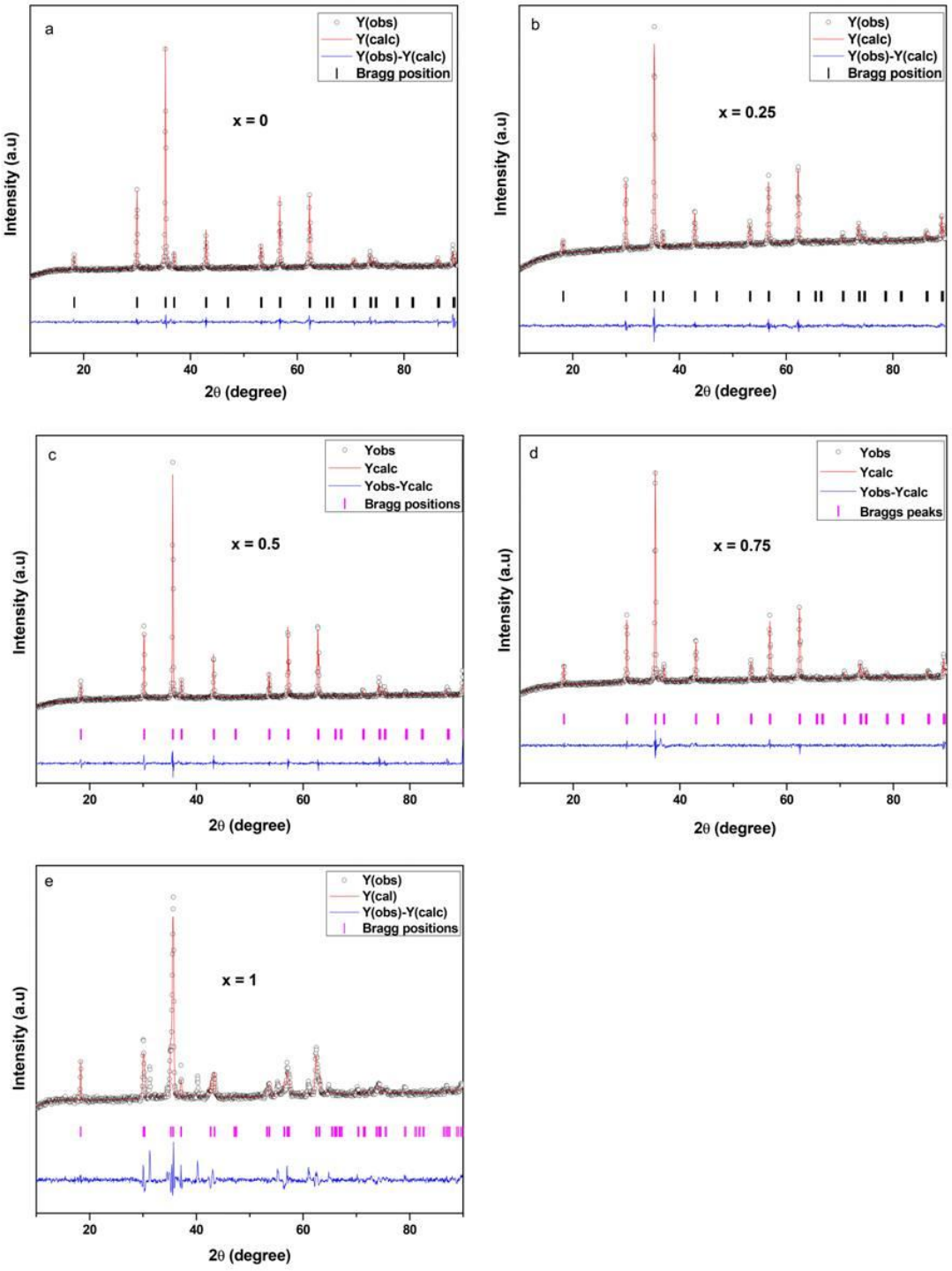

Figure 2 (a to e). Retvield Refinement of $Cu_x Zn_{1-x} Fe_2O_4$ (x=0, 0.25, 0.5, 0.75, 1)

$$Dnm = \frac{0.9\,\lambda}{\beta cos\,\theta} \qquad (1)$$

Where D_{nm} is the crystallite size (nm), λ is the incident X-ray wavelength (nm), θ is the Bragg's angle (degree), and β is the breadth of the primary peak at FWHM (radian).

The crystal size is different using different experimental methods [10]. In our study, the crystal size is maximum at $Cu_{0.5}Zn_{0.5}Fe_2O_4$, and the remaining crystals decrease while increasing doping concentration.

As shown in Figure 2, continuous XRD refinement was used until convergence was achieved, and the goodness factor was extremely near to 1. The values R_p, anticipated values (R_{exp}), discrepancy factor (R_{wp}) with the goodness of fit index (x^2), lattice parameters a, b, c, and volume, and density are presented in Table 1.

Table 1. The discrepancy factors and expected values, lattice parameters, volume, density, crystal size.

Sample	R_p	R_{wp}	R_{exp}	χ^2	a(A^0)	b(A^0)	c(A^0)	c/a	volume	Density(ρ) g/cm^3	Crystal size (D_{nm})
$ZnFe_2O_4$	40	14.9	9.42	2.47	8.426	8.426	8.426	1	598.395	5.166	38.78
$Cu_{0.25}ZnFe_2O_4$	41.5	14.5	10.26	1.99	8.431	8.431	8.431	1	599.379	5.760	35.19
$Cu_{0.5}Zn_{0.5}Fe_2O_4$	44	17.7	9.56	3.43	8.368	8.368	8.368	1	586.072	5.204	42.39
$Cu_{0.75}Zn_{0.25}Fe_2O_4$	42.5	14.6	10.3	1.98	8.413	8.413	8.413	1	595.631	5.040	39.09
$CuFe_2O_4$	65.4	29.3	12.5	5.47	5.9	5.9	8.478	1.43	295.192	6.111	38.91

The goodness of fit index $\chi^2 = (R_{wp}/R_{exp})^2$.

3.2. UV-VIS studies.

The $Cu_xZn_{(1-x)}Fe_2O_4$ Samples UV-VIS spectra were recorded at room temperature in the 200–800 nm range. According to the absorbance result, pure zinc ferrite exhibited a notable absorption in the UV and visible regions between 300 and 495 nm. Still, Cu-doped zinc ferrite revealed the UV region's highest absorption in the 300–500 nm range shown in Figure 3. The sample's optical band gap was calculated using the Tauc connection.

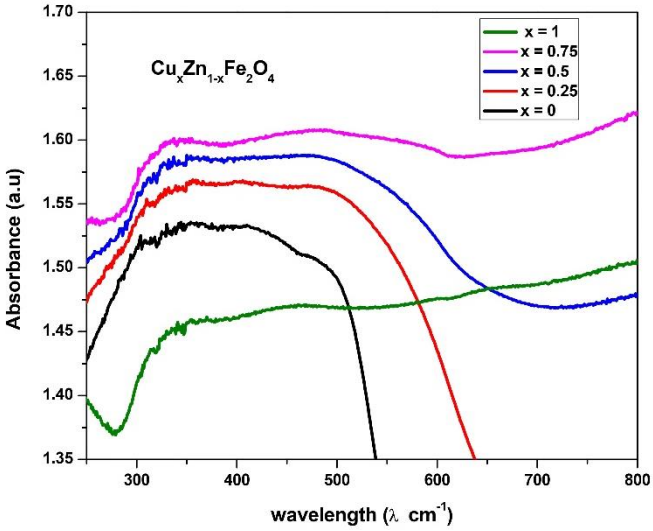

Figure 3. UV–visible absorption spectra of Cu_x $Zn_{(1-x)}Fe_2O_4$ (x = 0, 0.25, 0.5, 0.75, 1).

$$Eg = 1240/A \qquad (2)$$

$$(\propto h\nu) = A\,(h\nu - Eg)½ \qquad (3)$$

where α is the absorption coefficient, hν is the photon energy, A is absorbance, and E_g is the energy band gap.

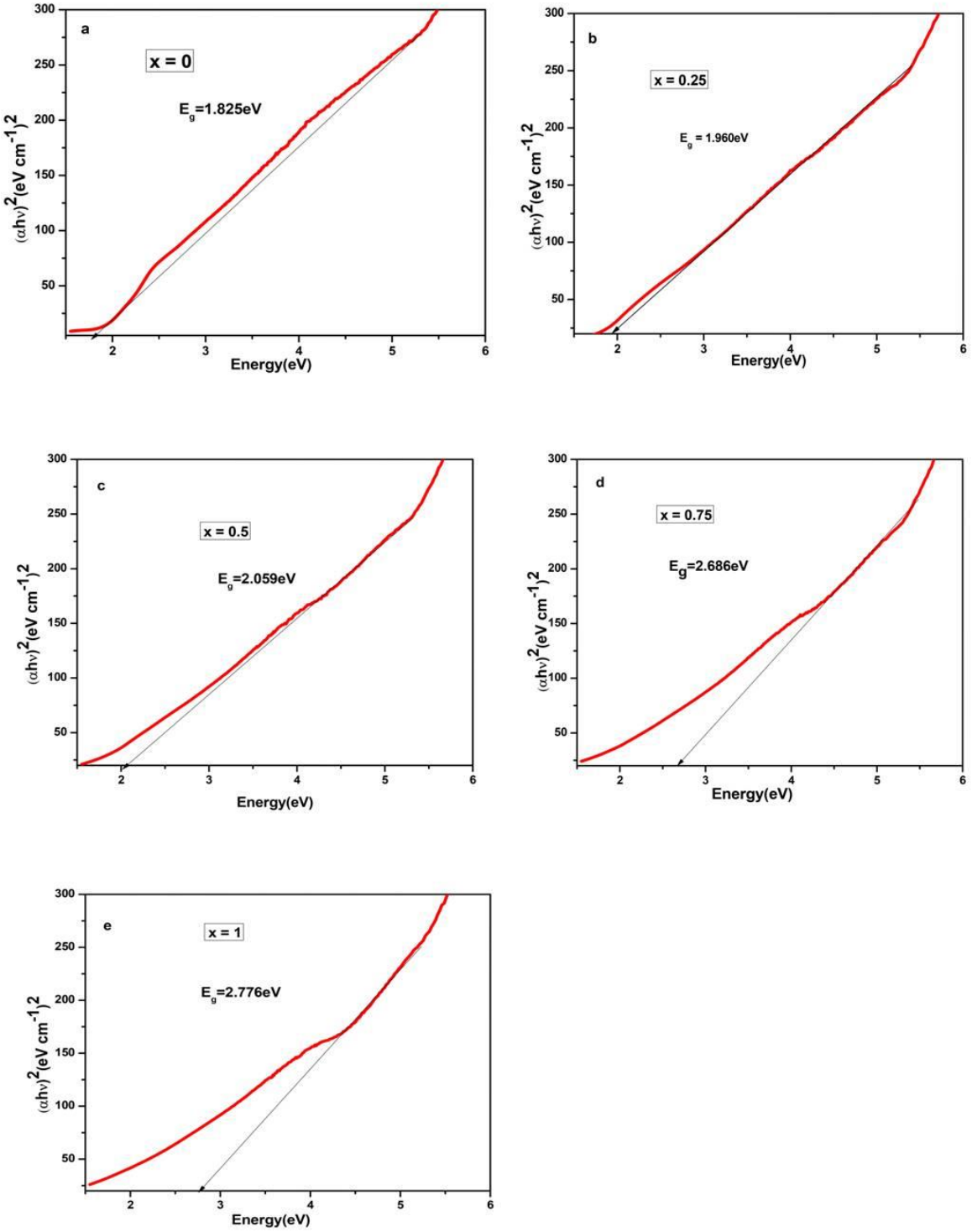

Figure 4 (a to e). Tauc plot $Cu_x Zn_{(1-x)}Fe_2O_4$ (x=0,0.25,0.5,0.75,1).

Figure 4 displays the $(\alpha h\nu)^2$ vs hν plot. For $ZnFe_2O_4$, $Cu_{0.25}Zn_{0.75}Fe_2O_4$, $Cu_{0.5}Zn_{0.5}Fe_2O_4$, $Cu_{0.75}Zn_{0.5}Fe_2O_4$, and $CuFe_2O_4$ the obtained band gap values are 1.825 eV, 1.960 eV, 2.059 eV, 2.686eV, and 2.776 eV respectively. While the wavelength of absorption shifts to a shorter wavelength and exhibits a blue shift, it is observed that the optical band gap increases with an increase in Cu concentration in the zinc ferrite system. This may be due to the decrease in crystal size, also reported [11]. The band gap decreased when crystal size increased in zinc-doped copper ferrite, which is related to the quantum confinement effect [12].

This may be due to the additional sub-bandgap energy levels caused by the combined surface and contact imperfections.

3.3. Raman spectroscopy.

Raman spectroscopy is used to measure the vibrational modes of $Cu_xZn_{(1-x)}Fe_2O_4$ (x = 0, 0.25, 0.5, 0.75, 1). Since the crystal structure is more visible in Raman spectra compared to XRD, room-temperature Raman spectra spaced between 100 and 800 cm^{-1} were obtained to determine the structural alterations resulting from Cu substitution in zinc ferrites Figure 5. In the current work, the cubic phase of copper-doped zinc ferrite converts into a tetragonal phase as the doping concentration increases. However, Cu substitution results in structural transitions from cubic (Fd-3m) to tetragonal (I41/amd) symmetry due to the weakening of the John-Teller distortion.

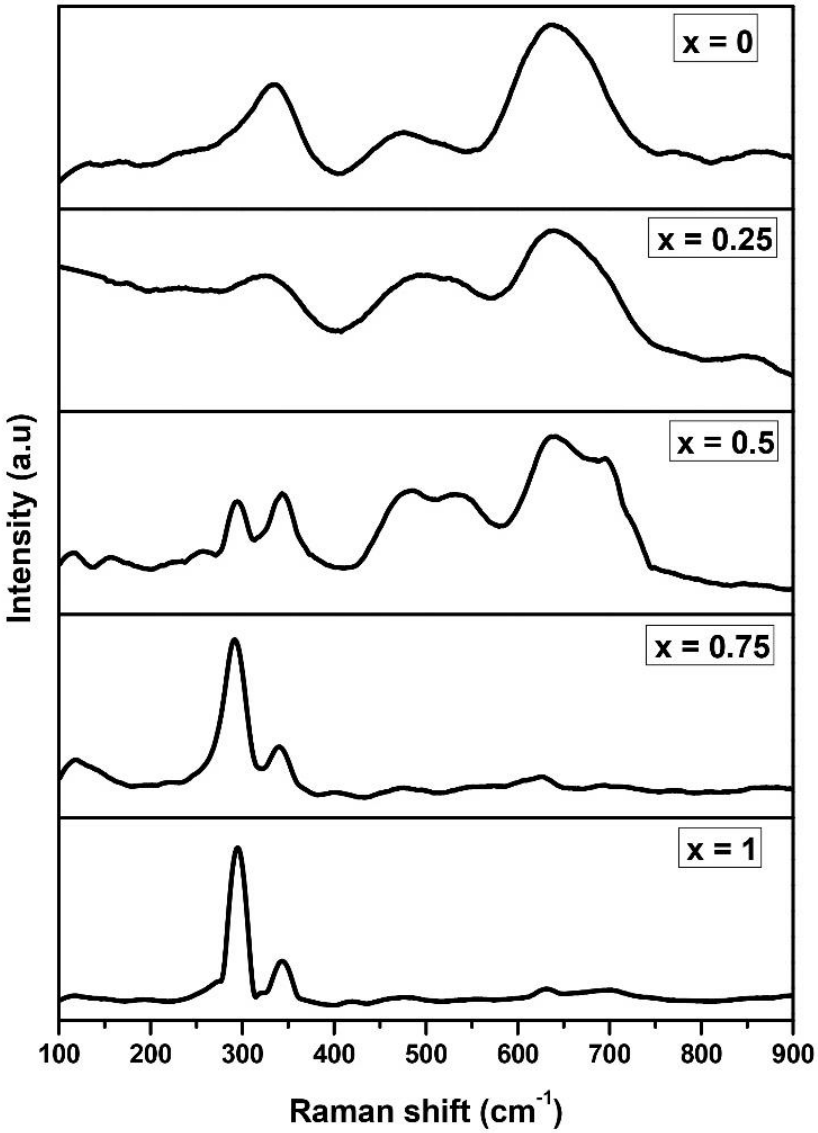

Figure 5. Raman spectra of $Cu_xZn_{1-x}Fe_2O_4$(x=0, 0.25, 0.5, 0.75, 1) at room temperature.

According to group theory, AB_2O_4 spinel ferrite in Raman spectroscopy exhibits 16 optical phonon modes with a cubic and Fd-3m space group. The five Raman modes (E_g+ $3T_{2g}$+A_{1g}) out of sixteen in the 200–800 cm^{-1} range confirm the cubic spinel phase. Below 600 cm^{-1} are the Raman modes linked to octahedral (BO_6) sub-lattice vibrations, whereas above

600 cm^{-1} are those related to tetrahedral (AO_4) sublattice vibrations. E_g denotes symmetric oxygen bending with respect to iron ions, T_{2g} denotes asymmetries in the stretching of Fe, and A_{1g} denotes symmetric stretching of oxygen atoms along Fe-O links. One-dimensional modes are represented by the notations A, T, and E, which stand for two and three-dimensional Raman modes, respectively.

Furthermore, the subscript g indicates the symmetry with respect to the center of inversion [13]. Ten Raman active modes confirm the tetragonal spinel phase, the I41/amd space group, for perfect A_{1g} +3B_{1g} +B_{2g} +4E_g [14]. Generally, the entire symmetric mode A_{1g} is found between 570 and 780 cm^{-1}, while the T_{2g} (3) and T_{2g} (2) are found between 350 and 400 cm^{-1} and 450 and 500 cm^{-1}, respectively. The other two low-frequency modes, Eg and F_{2g} (1), have less than 300 cm^{-1} frequencies and can occasionally be visible.

Table 2. Raman active modes of Cu_x $Zn_{1-x}Fe_2O_4$ (x=0.25,0.5,0.75,1).

Sample Names	A_{1g}(1)	A_{1g}(2)	B_g	T_{2g}(1)	E_g	T_{2g} (2)	T_{2g}(3)
Zn Fe_2O_4	643.8	681.99	----	141.19	319.04	352.99	483.89
$Cu_{0.25}Zn_{0.75}$ Fe_2O_4	649.94	----	102.21	165.85	249.59	328.99	494.55
$Cu_{0.5}Zn_{0.5}$ Fe_2O_4	640.67	696.36	122.44	248.22	294.55	342.99	500.41
$Cu_{0.75}Zn_{0.25}$ Fe_2O_4	620.47	----	121.34	291.71	341.85	75.01	525.05
Cu Fe_2O_4	115.49	295.35	343.76	390.59	76.74	631.24	691.80

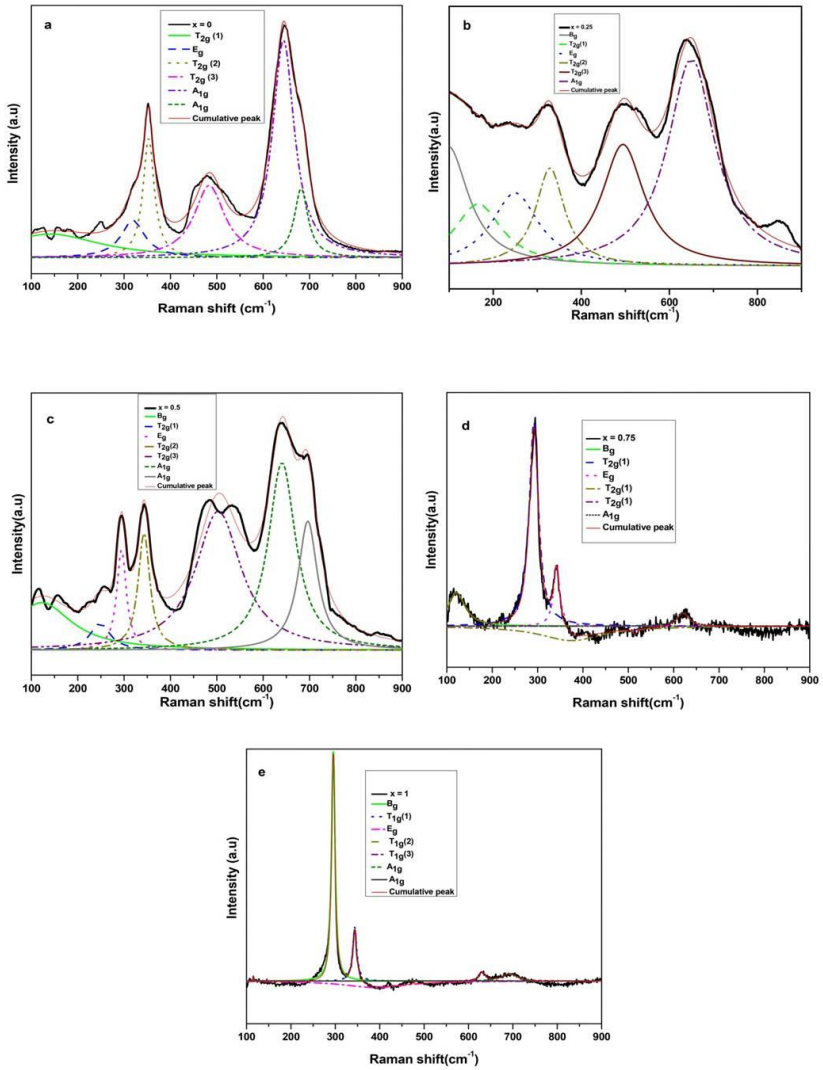

Figure 6 (a to e). Deconvoluted Lorentz Raman peaks of $Cu_xZn_{1-x}Fe_2O_4$(x=0, 0.25, 0.5, 0.75,1).

According to classical group theory, the following modes with cubic spinel structure correspond to the space group Fd3m, as per the earlier studies [15, 16] $A_{1g}(R) + E_g(R) + F_{1g} + 3F_{2g}(R) = \Gamma$ is equal to $A_{2u} + 2E_u + 4F_{1u}$ (IR) + $2F_{2u}$. In this case, A_{1g}, E_g, and $3T_{2g}$ are first order [17]. In Raman spectra, the modes of vibration around 490 cm^{-1} are characterized by the T2g (3) mode (asymmetric bending of oxygen), the modes at 340 are initiated by the T_{2g} (2) mode (asymmetric stretching of the (Fe/Cu/Zn)–O bond), and the modes reported by [18] are prompted by the A_{1g} mode (symmetric breathing mode of the AO_4 unit with spinel lattice). The related modes are shown in Table 2.

The spectra of all the samples under examination were acquired with a laser source operating at 633 nm. The deconvoluted Lorentz peaks from which the Raman peaks were are displayed in Figure 6 (a to e). According to [16], phase transition, cation distribution [19, 20], and distortion are all connected to the observed variations in Raman peaks. Lower wavenumber modes in the 460–660 cm^{-1} region are brought on by (Moct–O) vibration at the octahedral sites, while higher wave number Raman modes in spinel ferrites above 600–720 cm^{-1} are ascribed to (Mtet–O) vibration at the tetrahedral sites [21]. At the annealed temperature, tetragonal copper ferrite systems [22] exhibited Raman modes, which were observed. In the current study, we found that zinc ferrite changed from cubic to tetragonal shape when the doping concentration of copper increased.

3.4. FTIR studies.

Employing FTIR, we investigated the vibrational characteristics of $Cu_xZn_{1-x}Fe_2O_4$ in the given study. This compound may be in the IR-active spectral bands ν_4 (300-200 cm^{-1}), ν_1 (630-540 cm^{-1}), ν_2 (525-390 cm^{-1}) and ν_3 (380-335 cm^{-1}). The ν_1 band is ascribed to the intrinsic stretching vibration of metal cations at the tetrahedral site, and the ν_2 band is associated with metal cations in the octahedral site. The bands ν_3 and ν_4, which are commonly detected in the far infrared region, are linked to complex vibrations involving 42 octahedral and tetrahedral sites [23].

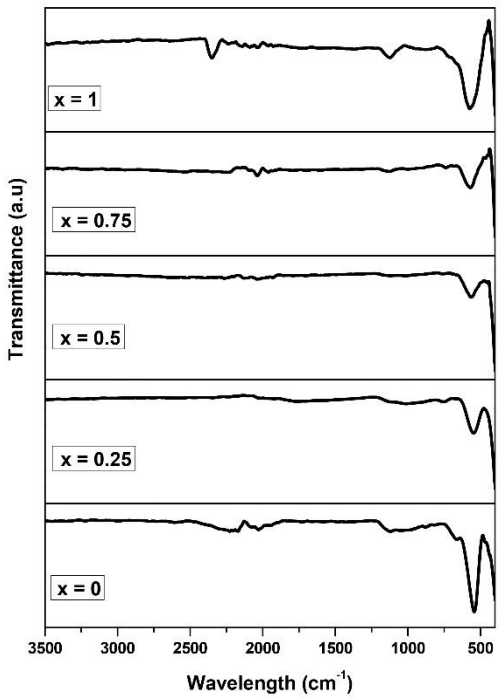

Figure 7. FTIR spectra of $Cu_xZn_{1-x}Fe_2O_4$(x=0,0.25,0.5,0.75,1).

Figure 7 shows how the ν_1 absorption bands spread and move towards higher frequencies with increasing copper content. These findings complement previous studies [24] that demonstrated that the bands shift toward a higher frequency range, and these bands are broader in copper ferrite [21]. The ν_1, ν_2, and other bands have cleared Figure. 8 (a to e), and additional bands are visible in Table 3. According to [25, 26] reports, zinc-doped copper ferrite was unannealed and annealed at 500°C and 600°C, respectively. Copper-doped Mg-Zn ferrite minimum and maximum bands with frequencies from 436-459 cm^{-1} and 617-555 cm^{-1} [27]. The stretching mode of vibrations in $CuFe_2O_4$ also identified organic groups in $ZnFe_2O_4$ [28, 29].

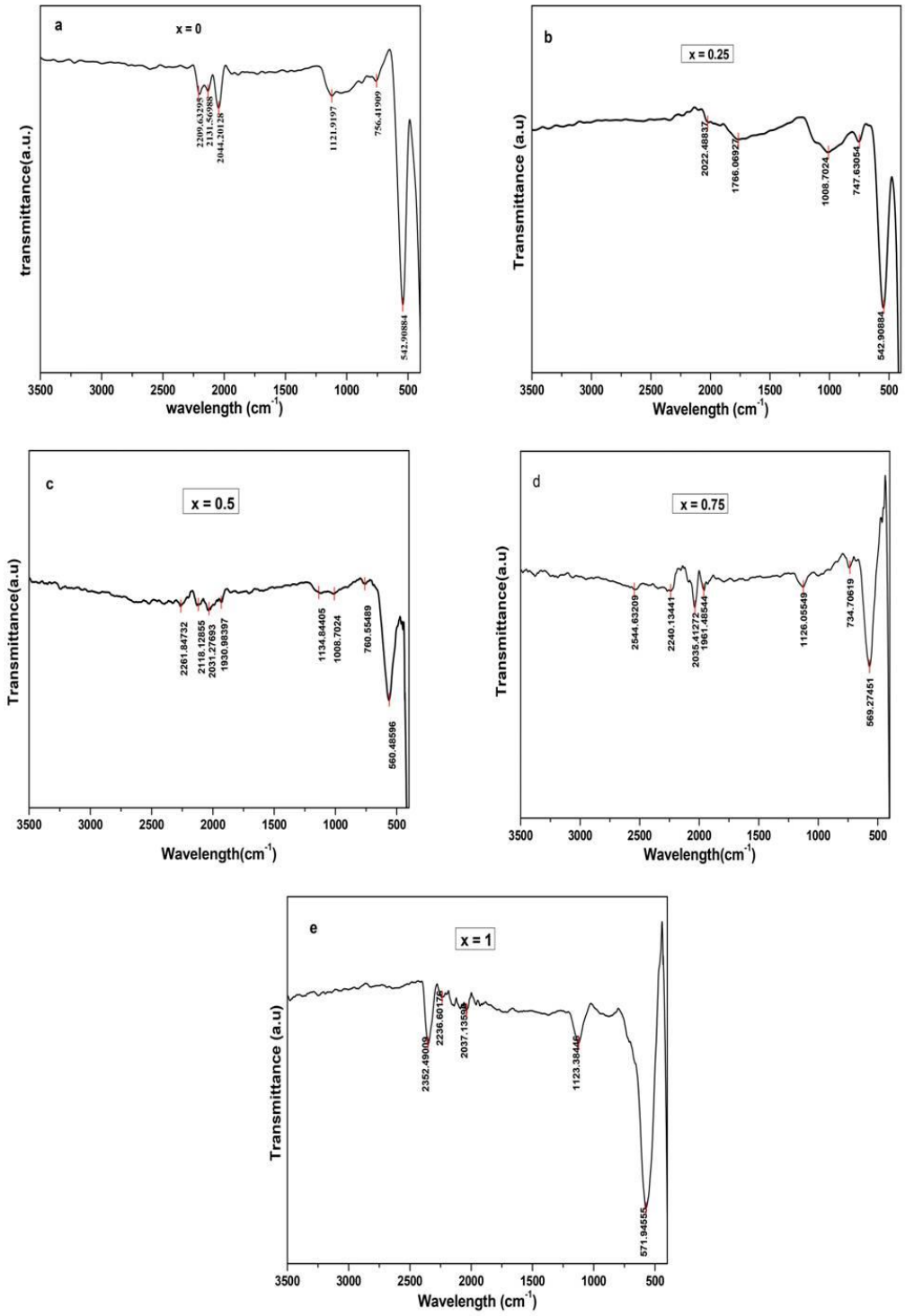

Figure 8. (a to e) FTIR spectra of $Cu_xZn_{1-x}Fe_2O_4$(x=0,0.25,0.5,0.75,1).

Table 3. IR bands of $Cu_xZn_{1-x}Fe_2O_4$(x=0, 0.25, 0.5, 0.75, 1).

Sample	Peaks of as prepared samples (cm^{-1})
$ZnFe_2O_4$	491.33, 542.90, 756.41, 1121.91, 2044.20, 2131.56, 2209.63
$Cu_{0.25}Zn_{0.75}Fe_2O_4$	424.97, 542.90, 747.63, 1008.70, 1766.06, 2022.48
$Cu_{0.5}Zn_{0.5}Fe_2O_4$	423.84, 560.04, 760.56, 1008.70, 1134.48, 1930.93, 2261.84
$Cu_{0.75}Zn_{0.25}Fe_2O_4$	410.65, 569.74, 734.70, 1126.05, 1961.48, 2035.41, 2544.63
$CuFe_2O_4$	410.32, 571.94, 1123.38, 2037.13, 2236.60, 2352.40

4. Conclusions

Copper doping in zinc ferrites leads to significant modifications in both structural and optical properties. XRD Rietveld refinement studies reveal changes in lattice parameters, density, volume, and crystallite sizes, for $Cu_{0.5}Zn_{0.5}Fe_2O_4$crystal size was more compared to all. At the same time, UV-Vis spectroscopy showed the highest optical absorption in the 300-500 nm and band gap energies from 1.825 eV to 2.776 eV. In XRD, we found that zinc ferrite changed from cubic to tetragonal shape when the doping concentration of copper increased, and it was confirmed in Raman's studies. The cation distribution was determined by integrating the intensities of deconvoluted Raman peaks. FTIR confirmed the tetrahedral site and octahedral site present in spinel ferrite. These findings enhance our understanding of the material's properties and could pave the way for optimizing copper-doped zinc ferrites for specific technological applications. Further studies could explore the magnetic properties and potential applications in photocatalysis or spintronics of copper-doped zinc ferrites, building on the insights gained from the structural and optical analysis.

Funding

This research received no external funding.

Acknowledgments

We thank Central Instrumentation Laboratory, University of Hyderabad, Hyderabad, Telangana, India, for their instrumentation support.

Conflicts of Interest

The authors declare no conflict of interest.

References

1. Aman, S.; Ahmad, N.; Alhossainy, M.H.; Albalawi, H.; Morsi, M.; Al-Muhimeed, T.I.; AlObaid, A.A. Structural, magnetic, electrical and microwave properties of spinel ferrites. *J. Rare Earths* **2022**, *40*, 443-450, https://doi.org/10.1016/j.jre.2021.04.015.
2. Li, Z.; Ying, Y.; Wang, N.; Zheng, J.; Yu, J.; Li, W.; Qiao, L.; Cai, W.; Li, J.; Huang, H.; Liu, Y. Effect of compressive stress on power loss of Mn–Zn ferrite for high-frequencyapplications. *Ceram. Int.* **2022**, *48*, 17723-17728, https://doi.org/10.1016/j.ceramint.2022.03.042.
3. Wang, N.; Ying, Y.; Zheng, J.; Li, W.; Qiao, L.; Cai, W.; Li, J.; Che, S. Development of Mn-Zn power ferrite with low losses over a broad temperature range for applications in the high frequency region of 0.5-3 MHz. *Ceram. Int.* **2021**, *47*, 21425-21432, https://doi.org/10.1016/j.ceramint.2021.04.152.

4. Liu, H.; Liao, J.; Li, C.; Huang, G. Contribution of Magnetization Mechanisms in MnZn Ferrites with Different Grain Sizes and Sintering Densification. *Coatings* **2024**, *14*, 302, https://doi.org/10.3390/coatings14030302.
5. Luo, F.; Duan, Z.; Zhang, Y.; Shang, Y. Influence of microstructure optimization on magnetic and thermal properties of MnZn ferrite. *J. Mater. Sci.: Mater. Electron.* **2021**, *32*, 15633-15642, https://doi.org/10.1007/s10854-021-06112-0.
6. Maria, K.H.; Choudhury, S.; Hakim, M.A. Structural phase transformation and hysteresis behavior of Cu-Zn ferrites. *Int. Nano Lett.* **2013**, *3*, 1-10, https://doi.org/10.1186/2228-5326-3-42.
7. Rahman, K.R.; Chowdhury, F.U.; Z.; Khan, M.N.I. Influence of Al^{3+} substitution on the electrical resistivity and dielectric behavior of Ni0. 25Cu0. 20Zn0. 55AlxFe2-xO4 ferrites synthesized by solid state reaction technique. *J. Magn. Magn. Mater.* **2017**, *443*, 366-373, https://doi.org/10.1016/j.jmmm.2017.07.098.
8. Patra, P.; Naik, I.; Kaushik, S.D.; Mohanta, S. Crossover from meta-magnetic state to spin-glass behaviour upon Ti-substitution for Mn in $CuMn_2O_4$. *J. Mater. Sci: Mater. Electron.* **2022**, *33*, 554-564, https://doi.org/10.1007/s10854-021-07326-y.
9. Calvo-de la Rosa, J.; SegarraRubí, M. Influence of the synthesis route in obtaining the cubic or tetragonal copper ferrite phases. *Inorg. Chem.* **2020**, *59*, 8775-8788, https://doi.org/10.1021/acs.inorgchem.0c00416.
10. Kumar, N.; Singh, D.; Nigam, A. ; Rajpoot, O.; Yadav, MK.; Singh, YP.; Prakash, PS.; Singh, S. Structural and magnetic properties of zinc doped copper ferrite synthesized by sol-gel and hydrothermal route. *Mater. Phys. Mech.* **2021**, *47*, 306-314, http://dx.doi.org/10.18149/MPM.4722021_12.
11. Nadhiya, D.; Kala, A.; Sasikumar, P.; Mohammed, M.K.A.; Thirunavukkarasu, P.; Prabhaharan, M.; Karnan, C.; Albukhaty, S.; Jabir, M.S.; Syed, A.; Elgorban, A. M.; Zaghloul, N.S.S. Influence of Cu^{2+} substitution on the structural, optical, magnetic, and anti bacterial behaviour of zinc ferrite nanoparticles. *J. Saudi Chem. Soc.* **2023**, *27*, 101696, https://doi.org/10.1016/j.jscs.2023.101696.
12. Hammad, T.M.; Salem, J.K.; Amsha, A.A.; Hejazy, N.K. Optical and magnetic characterizations of zinc substituted copper ferrite synthesized by a co-precipitation chemical method. *J. Alloy Compd.* **2018**, *741*, 123-130, https://doi.org/10.1016/j.jallcom.2018.01.123.
13. Sowjanya, P.; Pavan Kumar, N.; Ganesh, K.; Ramana Reddy, M. V. Analysis of Raman, Mossbauer Spectra and Dielectric Behaviour of Sol-Gel Prepared $Ni_{1-x}Co_xFe_2O_4$ Spinel Ferrites. *ECS J. Solid State Sci. Technol.* **2022**, *11*, 083008, https://doi.org/10.1149/2162-8777/ac869e.
14. Pramanik, P., Singh, S., Chowdhury, M.R., Ghosh, S., Sathe, V., Rabe, K.M., Vanderbilt, D., Seehra, M.S. and Thota, S. Lattice dynamics and magnetic exchange interactions in $GeCo_2O_4$: A spinel with S= 1/2 pyrochlore lattice. *Phys. Rev. B* **2021**, *104*, 014433, https://doi.org/10.1103/PhysRevB.104.014433.
15. Diab, R.S., El-Deen, L.M.S., Nasr, M.H., El-Hamalawy, A.A. and Abouhaswa, A.S. Structural, cation distribution, Raman spectroscopy, and magnetic features of Co-doped Cu–Eu nanocrystalline spinel ferrites. *J. Mater. Sci.: Mater. Electron.* **2024**, *35*, 290, https://doi.org/10.1007/s10854-024-12047-z.
16. Albini, B.; Restelli, S.; Ambrosetti, M.; Bini, M.; D'Amico, F.; Mozzati, M.C.; Galinetto, P. Raman spectroscopy in pure and doped zinc ferrites nanoparticles. *J. Mater. Sci.: Mater. Electron.* **2023**, *34*, 1030, https://doi.org/10.1007/s10854-023-10464-0.
17. Sarkar, B.J.; Kundu, M.; Mondal, B.; Mukherjee, S.; Bandyopadhyay, A.; Roy, U.K. Microstructural investigation of sonochemically synthesized Zn substituted $CuFe_2O_4$ nanoparticles for heterogeneous green catalytic click chemistry and dye degradation. *J. Mol. Struct.* **2023**, *1274*, 134493, https://doi.org/10.1016/j.molstruc.2022.134493.
18. Tandon, V.; Saleem, M.; Kaurav, N.; Dixit, R.C. Influence of barium (Ba^{2+}) doping for Cu-Zn ferrites on structural and electrical properties. *Mater. Today Proc.* **2020**, *30*, 234-237, https://doi.org/10.1016/j.matpr.2020.06.520.
19. Nakagomi, F.; de Souza, P.E.N.; Castro, T.J.; Garg, V.K.; Oliveira, A.C.; e Silva, F.C.; Franco Jr, A.; Morais, P.C. da Silva, S.W. Cation distribution of $Zn_xCo_{1-x}Fe_2O_4$ nanoparticles: A resonant X-ray diffraction study. *J Alloy Compd.* **2020**, *842*, 155751, https://doi.org/10.1016/j.jallcom.2020.155751.
20. Vatsalya, V.L.S.; Sundari, G.S.; Sridhar, C.S.; Lakshmi, C.S. Evidence of super paramagnetism in nano phased copper doped nickel zinc ferrites synthesized by hydro thermal method. *Optik* **2021**, *247*, 167874, https://doi.org/10.1016/j.ijleo.2021.167874.
21. Dhyani, R.; Srivastava, R.C.; Rawat, P.S.; Dixit, G. Structural and elastic properties of tetragonal nano-structured copper ferrite. *IJMR* **2022**, *113*, 884-892, https://doi.org/10.1515/ijmr-2021-8552.

22. Sefatgol, R.; Gholizadeh, A. The effect of the annealing temperature on the microstructural, magnetic, and spin-dynamical properties of Mn–Mg–Cu–Zn ferrites. *PhysB: Condens* **2022**, *624*, 413442, https://doi.org/10.1016/j.physb.2021.413442.
23. Paunović, N.; Dohčević-Mitrović, Z.; Djokić, D.M.;Aškrabić, S.;Lazović, S.; Abraham, A.R.; Raneesh, B.; Kalarikkal, N.; Thomas, S. Revealing plasmon-phonon interaction in nanocrystalline $MgFe_2O_4$ spinels by far-infrared reflection spectroscopy. *Mater. Sci. Semicond. Process* **2022**, *149*, 106889, https://doi.org/10.1016/j.mssp.2022.106889.
24. Pund, S.N.; Nagwade, P.A.; Nagawade, A.V.; Bagade, A.V. Influence of Cu^{2+} substitution on structural and optical properties of Mg-Zn ferrite nanoparticles. *Mater. Today Proc* **2022,** *49*, 2382-2391, https://doi.org/10.1016/j.matpr.2021.09.402.
25. Ati, A.A.; Abdalsalam, A.H.; Abbas, H.H. Influence of annealing on structural, morphology, magnetic and optical properties of PLD deposite $CuFe_2O_4$ thin films. *Inorg. Chem. Commun.* **2022**, *146*, 110072, https://doi.org/10.1016/j.inoche.2022.110072.
26. Kothapally, S.; Kotru, S.; Paul, R.; Abu Qahouq, J.A. Optical studies of pure and (Cu, Co) doped nickel zinc ferrite films deposited on quartz substrate. *JVSTA* **2023**, *41*, https://doi.org/10.1116/6.0002262.
27. Ramanjaneyulu, K.; Suryanarayana, B.; Raghavendra, V.; Murali, N.; Parajuli, D.; Chandramouli, K. Synthesis, microstructural and magnetic properties of Cu doped $Mg_{0.5}Zn_{0.5}Fe_2O_4$ ferrites. *Solid State Technol.* **2021**, *64*, 7192-7200, https://www.researchgate.net/publication/352063656.
28. Priyadharsini, R.; Venkateshwarlu, M.; Deenadayalan, K.; Manoharan, C. The influence of reaction and annealing temperature on physical and magnetic properties of $CuFe_2O_4$ nanoparticles: Hydrothermal method. *Inorg. Chem. Commun.* **2022**, *140*, 109406, https://doi.org/10.1016/j.inoche.2022.109406.
29. Sundararajan, M.; Sukumar, M.; Dash, C.S.; Sutha, A.; Suresh, S.; Ubaidullah, M.; Al-Enizi, A.M.; Raza, M.K.; Kumar, D. A comparative study on $NiFe_2O_4$ and $ZnFe_2O_4$ spinel nanoparticles: structural, surface chemistry, optical, morphology and magnetic studies. *Phys. B: Condens.* **2022**, *644*, 414232, https://doi.org/10.1016/j.physb.2022.414232.